

Imaging Black Holes with Simulated Space Expansions to the Event Horizon Telescope

by

Daniel Palumbo

Submitted to the Department of Physics
in partial fulfillment of the requirements for the degree of **ARCHIVES**

Bachelor of Science in Physics

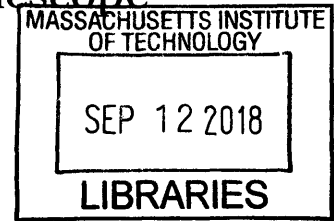
at the

MASSACHUSETTS INSTITUTE OF TECHNOLOGY

June 2018

© Smithsonian Institution, 2018. All rights reserved.

The author hereby grants to MIT permission to reproduce and to
distribute publicly paper and electronic copies of this thesis document
in whole or in part in any medium now known or hereafter created.



Signature redacted

Author
Department of Physics

Signature redacted

May 11, 2018

Certified by.....
Doctor Sheperd Doeleman
Assistant Director of Observation, Black Hole Initiative
Thesis Supervisor

Signature redacted

Certified by.....
Professor Nevin Weinberg
Associate Professor, Department of Physics
Thesis Supervisor

Signature redacted

Accepted by
Professor Scott Hughes
Interim Physics Associate Head, Department of Physics

Imaging Black Holes with Simulated Space Expansions to the Event Horizon Telescope

by

Daniel Palumbo

Submitted to the Department of Physics
on May 11, 2018, in partial fulfillment of the
requirements for the degree of
Bachelor of Science in Physics

Abstract

The Event Horizon Telescope (EHT) is a multinational Very-Long-Baseline Interferometry (VLBI) network of dishes joined to resolve general relativistic behavior near a supermassive black hole. The imaging quality of the EHT is largely dependent upon the sensitivity and spatial frequency coverage of the many baselines between its constituent telescopes. The EHT already contains many highly sensitive dishes, including the crucial Atacama Large Millimeter/Submillimeter Array (ALMA), making it viable to add smaller, cheaper telescopes to the array, greatly improving future capabilities of the EHT. We explore the feasibility of adding small orbiting dishes to the EHT, and develop orbital optimization tools for space-based VLBI imaging. Unlike the Millimetron mission planned to be at L2, we specifically treat low and medium Earth orbiters which rapidly fill spatial frequency coverage across a large range of baseline lengths. Finally, we demonstrate significant improvement in image quality when adding small dishes to planned arrays in simulated observations of both SgrA* and M87.

Thesis Supervisor: Doctor Sheperd Doeleman
Title: Assistant Director of Observation, Black Hole Initiative

Thesis Supervisor: Professor Nevin Weinberg
Title: Associate Professor, Department of Physics

Acknowledgments

I would like to acknowledge my two supervisors, Dr. Sheperd Doeleman and Prof. Nevin Weinberg, for their constant support throughout my junior and senior years at MIT. My beloved Event Horizon Telescope collaborators are too numerous to thank, but I would like to specifically mention Dr. Michael Johnson, Dr. Katie Bouman, Andrew Chael, and Dr. Lindy Blackburn. They have all been crucial to my understanding of very-long-baseline Interferometry and to my development as a researcher.

The material in this thesis is largely drawn from an upcoming paper[40] by Palumbo, Doeleman, Johnson, Bouman, and Chael based on work done by Event Horizon Telescope collaborators at the Smithsonian Astrophysical Observatory.

Contents

1	Introduction	13
1.1	Very Long Baseline Interferometry	14
1.1.1	A Brief History of Radio Interferometry	15
1.1.2	VLBI Data Reduction and Fourier Synthesis	19
1.2	The Event Horizon Telescope	21
1.2.1	Observation Targets	22
1.2.2	EHT Array Sites in 2018	22
2	Motivation for Space Expansion of the Event Horizon Telescope	25
2.1	Signal to Noise Ratio	25
2.2	Fourier Coverage	27
2.2.1	Orbit Design and Simulation	27
2.3	Imaging	31
2.3.1	Imaging SgrA*	32
2.3.2	Imaging M87	33
3	Numerical Constraints on Space-Based Observation	37
3.1	Integration Time	37
3.1.1	SNR and Noise on Strong Baselines	37
3.1.2	Motion Blurring	39
3.2	Hardware Specifications	40
3.2.1	Local Oscillators	40
3.2.2	Antenna Surface	41

4 Conclusion and Paths Forward	43
A EHT Station Parameters	45

List of Figures

1-1 Fourier coverage of the EHT 2018 Array if observing at 345GHz. . . . 24

2-1 Example orbiter positions and (u, v) coverage of SgrA* with 4 orbiters. Positions are shown once per minute over six hours of observation starting at 0 GMST. 29

2-2 Simulated static and dynamical imaging of 2 hour observations of SgrA* with phase-coherent EHT and space dishes at .87 mm. A 16 GHz bandwidth and 30 second integration time are assumed for each individual observation, advancing 30 seconds between observations. The first row are reconstructions of a static crescent; the second are frames from movies of an orbiting "hot spot" model of SgrA* with a period of 30 minutes. 33

2-3 Simulated static of 90 minute observations of SgrA* with phase-coherent ground-enhanced EHT and space dishes at .87 mm. A 16 GHz bandwidth and 30 second integration time are assumed for each individual observation, advancing 30 seconds between observations. 34

2-4	Single frames from dynamical reconstructions of 3-hour synthetic observations of simulated M87 jet motion. A mask composed of all non-zero values in the simulation has been applied to the fit space in the reconstructions. At top, the input video. At center, reconstructing from observations with the EHT2018. At bottom, the EHT2018 + 4x4m orbiting dishes. The addition of orbiting dishes allows the correct reconstruction of outflow structures and eliminates most of the erroneous rippling structure in the synthetic EHT2018 simulation. . .	35
3-1	Fourier coverage over 1.5 hours of a simulated hotspot[7] of SgrA* at .87 mm by the EHT 2018 array when four, four-meter dishes in low Earth orbit are added to the array, viewed after accounting for the ensemble-average blurring by the scattering kernel towards SgrA*. Ground-ground baselines are shown in purple, while space-ground baselines are shown in the orange gradient, scaling with SNR.	38
3-2	Ruze formula plotted for observation at .87 mm (lower curve) and 1.3 mm (higher curve).	42

List of Tables

A.1	Estimated EHT Station Parameters in 2018.	45
-----	---	----

Chapter 1

Introduction

Black holes are the most mysterious objects in the universe. They are one of the most extreme predictions of Einstein's theory of General Relativity; theoretical and observational understanding of black holes has been a primary goal in the field of astrophysics since they were first predicted. The laws of physics seem to break down at the boundary of a black hole, the event horizon - a region beyond which gravity is so strong that not even light can escape its pull.

Despite this perfect darkness, black holes are observable. Black holes are expected to be at the centers of most galaxies, and their gravitational pull on nearby stars leads to rapid, highly eccentric orbits near galactic nuclei, as has been observed near SgrA* [23]. However, even in the immediate vicinity of a black hole, we expect to see bright emission, as accreting gas heats up and glows[16] during in-fall.

Observing this emission near the event horizon is the goal of the Event Horizon Telescope, or EHT, an international collaboration of astronomers using a global network of radio telescopes to observe supermassive black holes with incredibly high angular resolution. To do so, the EHT uses the technique of Very Long Baseline Interferometry, or VLBI, correlating the output of physically disparate telescopes to gain information about the target intensity distribution as though observing with an aperture as wide as the Earth. In particular, the EHT has singled out Sagittarius A* (SgrA*) and Messier 87 (M87) as productive observational targets due to their large apparent size and the compelling science attainable from imaging these targets.

In this thesis, we explore a possible future path for the Event Horizon Telescope. We consider the feasibility of adding space-based dishes to the VLBI network. Space dishes in low- or medium-Earth orbit provide significant benefits to imaging due to their rapid forming of baselines to ground dishes at many different lengths and orientations, as will be discussed in detail later. Further, the EHT plans to increase its observing frequency to 345 GHz in the future. Performing VLBI at this incredibly high frequency requires precise timing and positional information, demanding careful hardware consideration for a rapidly moving space dish. Further, we use simulated data from a hypothetical space-enabled EHT to form images with EHT-standard imaging algorithms, forming both static images and dynamic movies of SgrA* and M87. Ultimately, we find that expansions to space are a compelling empowerment to the imaging capabilities of the EHT, and that corresponding technological development would be an immense asset to the VLBI efforts of the next several decades.

1.1 Very Long Baseline Interferometry

Very Long Baseline Interferometry is the natural result of one of the core motivations in observational astronomy: the drive to see finer detail, to look more closely at the sky. One need look no further than the most basic scaling relation in any astronomer's arsenal, that for angular resolution, to see the power of interferometry:

$$\theta_{\text{R}} \approx \frac{\lambda}{D} \tag{1.1}$$

An observer can only distinguish two points of light if they are separated by an angle of at least θ_{R} given by the ratio between the observing wavelength λ and the aperture diameter D . To resolve finer detail, one must decrease λ or increase D . There are additional constraints on the observing wavelength, such as the emission spectrum of the target, and what intermediate scattering may affect the signal. The aperture diameter is constrained by more immediately accessible demands, such as the size we can build our telescopes while maintaining good surface accuracy.

VLBI presents a tantalizing notion: if the output of two telescopes can be com-

bined such that the effective aperture diameter is instead the baseline distance between them, then incredibly high angular resolution can be achieved using a network of telescopes. Assuming only ground telescopes are used, there is a natural upper bound on this distance: the maximum distance between two points on the Earth that are still visible from a point source at infinity is the diameter of the Earth, a bound which the Event Horizon Telescope nearly saturates.

For a full treatment of interferometry in radio astronomy, the author recommends Thompson, Moran, and Swenson’s *Interferometry and Synthesis in Radio Astronomy* [51], the central text of modern VLBI. However, for the purposes of understanding the core arguments of this thesis, we provide a brief historical overview of previous VLBI undertakings, as well as a summary of the basic parameters of VLBI observation and imaging.

1.1.1 A Brief History of Radio Interferometry

Michelson pioneered astronomical interferometry with his work on stellar observations in the optical regime [36], dating back to the end of the 19th and early 20th century. Though Michelson was not using radio telescopes or greatly separated apertures, the underlying mathematics generalized to longer wavelengths, enabling the later observations [46] of the sun by Ryle and Vonberg, which used a pair of radio antennas.

The modern analytical vocabulary of VLBI took shape after World War II, as coastal radio antennas in Australia initially used for radar were repurposed to form interference fringes [35] between solar radio signals and their counterparts after reflection from the ocean surface. The use of Fourier synthesis to compute source intensity from fringe measurements is the core process of all of modern VLBI analysis.

However, it was not until Ryle introduced phase-switching interferometry [43] that fringe oscillation could be isolated from the rest of the receiver output, reducing the sensitivity of the measurement to gain variation at each constituent instrument. More generally, Ryle introduced the use of voltage correlation to the interferometric signal path, which is still central to VLBI data reduction pipelines today.

Also relevant today is the use of calibration sources for antenna pointing, which

relies on sources with well-known positions that are bright both optically (for high position precision) and in the radio (for antenna pointing). This practice was pioneered in the 1950s by Smith [47, 48], and allowed antenna calibration to be performed relative to low-uncertainty positions as more calibration sources were discovered.

The 1950s also saw the use [37, 49] of the magnitude of measured interference fringes to calculate the angular widths of radio sources. In general, interferometers measure spatial Fourier components along the axis of their constituent element separation. Thus, the source intensity distribution is related to the measured fringes by a Fourier transform.

However, a slightly different approach was pioneered by Jennison and Das Gupta, also working on the angular width problem. Correlating the intensity of spaced detectors yields an intensity in the visibility domain [11] that is proportional to the conventional interferometer visibility, squared. Though intensity interferometry is not in use today, particular measurements [27, 28] demonstrated a source model degeneracy that could be broken only by fringe phase information not provided by an intensity interferometer apparatus. A follow-up experiment [29] using a conventional interferometer with three antennas yielded this phase information, but more importantly, pioneered the use of instrument- and atmosphere-invariant closure quantities [26] in radio interferometric analysis. The closure phase developed by Jennison is extremely robust, and is popular in modern analysis techniques, including those developed within the Event Horizon Telescope [12] at the cutting edge of VLBI imaging.

A long line of incremental improvements and explorations within the broad field of radio interferometry followed throughout the latter half of the 20th century. Among them, the technique most crucial to the Event Horizon Telescope is Earth-rotation synthesis imaging. As we have found in our tour through the history of radio interferometry, one can partially reconstruct a source intensity distribution by finding interferometric fringes between two antennas. The information gained about the source is dependent upon the length and orientation of the separation vector between the two dishes. As the Earth rotates, a pair of dishes on the Earth's surface will sweep through a smooth curve of relative positions, allowing a range of orientations

and separation lengths to accumulate for a single interferometer. O'Brien [39] was one of the first to employ this for solar observations, followed soon after by Christiansen and Warburton [14]. The first non-solar Earth-rotation interferometry was performed by Rowson [42], though the most important foray into the use of this technique came with the construction of the Cambridge One-Mile Telescope. Ryle et al. produced images [45] of Cygnus A and Cassiopeia A with incredible angular resolution and began the march of synthesis imaging development.

The success of the Cambridge One-Mile Telescope increased investment into arrays of antennas that would provide more comprehensive Fourier sampling of a number of radio observation targets. Interferometers like the National Radio Astronomy Observatory's Green Bank instrument [25] were reconfigured for optimal use in Fourier synthesis imaging. The 1970s saw the construction of a number of powerful arrays, notably the Five-Kilometer Radio Telescope in England [44], the Westerbork Synthesis Radio Telescope in the Netherlands [2], and the Very Large Array in New Mexico [50]. These arrays were each designed with similar guiding principles; the number of interferometric pairs or "baselines" in the array grows quadratically with the number of dishes, so an array of many dishes at a variety of separations at the kilometer scale will provide robust Fourier coverage that grows as the Earth rotates, enabling rapid measurement of the visibility function of the source at the observed wavelength. These arrays could observe at wavelengths of centimeters, and could form images with angular resolution on the order of 1 arcsecond.

The most powerful such local array interferometer in operation today is the Atacama Large Millimeter Observatory [54], or ALMA. The array consists of two sub-arrays which can be arranged in a variety of configurations depending on the operating mode and observational target. The primary sub-array contains 50 12-m antennas, while the secondary compact array contains 12 7-m antennas. ALMA has an angular resolution of approximately 0.1 arcsecond, making it the highest-resolution local radio observing apparatus in the world. ALMA was recently upgraded to phased-array operation, allowing it to operate as a single, powerful dish in a greater VLBI array.

So far, the interferometers we have discussed involved elements that were some-

what close together, with the largest separation less than 20 kilometers. These are connected-element interferometers; with few exceptions, individual dishes in these arrays have their output correlated immediately upon readout. However, as always, interferometry teases us with the possibility of incredible angular resolution with incredible baseline lengths. To correlate the output from telescopes on opposite sides of the world, the signals from each dish need to be stored with high fidelity for later correlation. This technique is known as very-long-baseline interferometry.

In general, VLBI requires the conversion of the received electromagnetic signal to a significantly lower intermediate frequency, or IF, amenable to the available amplification and recording media at the desired bandwidth. This methodology was present even in the earliest consideration and practice of VLBI [10, 8, 9] in the late 1960s. VLBI proceeded to grow in popularity due to its usefulness in geodetics [53] and the incredible angular resolution that Earth-size baselines provide: on the order of tens to hundreds of micro arcseconds at high radio frequencies. Continued investment in VLBI and in related disciplines led to better frequency and positional standards that enabled VLBI at higher and higher frequencies; the Event Horizon Telescope pushes the envelope of modern VLBI by using telescopes around the world observing at 230 GHz with planned operation at 345 GHz.

VLBI benefits particularly well from the existence of ALMA for reasons that we will explore in greater mathematical detail later; simply put, an interferometric baseline's sensitivity scales with the geometric mean of the sensitivities of its two constituent telescopes. Thus, the completion of the phased-array operating mode of ALMA [34] has ushered in a new era of feasibility for small dishes that would otherwise not be useful for VLBI, but can form fringes with ALMA. Exploring this feasibility is the primary motivation for this thesis; in space, antenna size places a far greater constraint on experiment design than on the ground due to the difficulty of launching large objects into orbit. ALMA's sensitivity allows small, relatively easy-to-launch orbiters to contribute to VLBI Fourier synthesis imaging.

That said, constructing Earth-space interferometers is not a brand new idea. The first Earth-space fringe detection [33] was in 1989, using the TDRSS system in geosta-

tionary orbit. Non-geostationary orbits sweep through much broader Fourier coverage and are not fundamentally limited in baseline length; in 1997, the VLBI Space Observatory Programme, or VSOP [24], brought the 8-m diameter Highly Advanced Laboratory for Communications and Astronomy (HALCA) into a highly elliptical Earth orbit with a period of approximately 6.6 hours and an apogee of 21,000 km. HALCA was followed shortly thereafter by the 10-m diameter RadioAstron (or Spektr-R) [32], which had a period of 8.6 days and an apogee of approximately 300,000 km. These dishes operated at centimeter wavelengths, and successfully detected fringes despite the difficulties of space-ground interferometry. The successes and struggles of these projects provide partial guidance for future efforts in orbiting VLBI, or OVLBI. As we consider the benefits of a significantly closer-to-Earth space mission for the Event Horizon Telescope, we will consider the lessons these missions have to offer. However, before we can begin to formulate a new antenna archetype for the EHT, we must first consider the analytical underpinnings of VLBI.

1.1.2 VLBI Data Reduction and Fourier Synthesis

For a full derivation of the mathematical relationships that underly interferometry, and further, VLBI, the author again points readers to Thompson, Moran, and Swenson’s *Interferometry and Synthesis in Radio Astronomy* [51]. Here, we will briefly review crucial results from a point of significant abstraction to get an intuition for the parameters of a VLBI observation, and the mathematical manipulation required to turn a network of electromagnetic field measurements into usable interferometric observables.

To begin with, consider what each telescope actually measures. An incoming electromagnetic plane wave from a distant source is read out in some well-characterized way as a time-dependent voltage. After down-mixing to an intermediate frequency suitable for the backend electronics, the signal is either correlated immediately (in the case of a connected-element interferometer) or stored on some data medium (in the case of VLBI). Either way, in the general case, the signal is correlated with that of a distant telescope to form an interference pattern. The characteristic interference

fringes arise from the path length difference between the two dishes. For two dishes on distant points on the surface of the Earth, this path length difference relies on the three-dimensional coordinates of both telescopes and the current rotational position of the Earth relative to the source.

Consider a source intensity distribution on the sky given by $I(l, m)$, where l and m are two orthogonal angles measured relative to a phase reference point on the sky. The Fourier transform of this distribution is the visibility $V(u, v)$, where u and v correspond to the spatial frequency components of the intensity distribution, and thus to a number of wavelengths. The (u, v) coordinate system is developed by considering the path from one of the two dishes to the source, a source vector we will call \vec{s} . A plane is defined by \vec{s} and the celestial pole. We define the v axis to be that which is perpendicular to \vec{s} in this new plane. Similarly, we may define the u axis to be the axis perpendicular to both \vec{s} and the v axis. We may further define the w axis along the line of sight \vec{s} , though it is not relevant to VLBI, as targets are assumed to be at infinity. Since observations occur at a known wavelength, w -axis interferometry does not provide any new information.

For the standard (X, Y, Z) coordinate system, which provides a right-handed Cartesian coordinate system for positions on Earth, (u, v, w) coordinates can be expressed as

$$\begin{bmatrix} u \\ v \\ w \end{bmatrix} = \frac{1}{\lambda} \begin{bmatrix} \sin H & \cos H & 0 \\ -\sin \delta \cos H & \sin \delta \sin H & \cos \delta \\ \cos \delta \cos H & -\cos \delta \sin H & \sin \delta \end{bmatrix} \begin{bmatrix} X \\ Y \\ Z \end{bmatrix}$$

for the hour angle H and declination δ .

Thus, the (u, v) coordinate system allows us to describe relative positions of telescopes in terms of the number of wavelengths between them, and thus which Fourier components of a source intensity distribution would be sampled by observation at a particular wavelength. Note that the Fourier coupling between the (u, v) and (l, m) coordinates means that larger antenna spacings, which are large vectors in (u, v) space, give information about the smaller scales of the sky intensity distribution. Thus, the minimum angular resolution of a particular array of dishes is set by the

largest antenna separation in units of wavelengths. This is fully consistent with our beginning intuition that the large effective diameter of a synthetic interferometric dish would yield an angular resolution capable of finding detail within point-like sources.

Intuitively, performing a Fourier transform on the samples of the $V(u, v)$ function yielded by interferometric observations yields a "dirty image" riddled with sidelobes as a result of the finite, partial coverage of the (u, v) plane afforded by an array of distant dishes with irregular spacings. Efforts to reconstruct images without the artifacts of the dirty image are a matter of ongoing research. The most famous such method, the CLEAN algorithm [25], subtracts out point-sources in the dirty image and replaces their beam response with a sidelobe-free response of the same magnitude. Though CLEAN has stood the test of time and is still in use by some Event Horizon Telescope collaborators, competing imaging methods with different approaches have also been successful in removing the artifacts from simple Fourier transformation. For the purposes of this paper, an instance of the Maximum Entropy method [13] developed by the EHT's own Andrew Chael is used. Chael's accompanying VLBI data manipulation and observation simulation library has been used to test varying VLBI arrays in different imaging scenarios.

1.2 The Event Horizon Telescope

The Event Horizon Telescope is a very-long-baseline interferometry array operating at very high radio frequencies (above 230 GHz) to observe and image supermassive black holes. Intuitively, high frequency operation is crucial to the incredible angular resolution of the array - approximately 15 microarcseconds - as the number of wavelengths of separation in a given baseline increases with frequency. Though most atmospheric effects get worse at lower wavelengths, scattering with the interstellar medium scales with λ^2 as detailed in [51], adding further incentive to operate in the microwave frequency regime. The EHT plans to upgrade to operation at 345 GHz (.87mm) in the next decade, further increasing the angular resolution of the array. As this thesis considers space expansions of the EHT that would occur on roughly the

same timescale as the frequency change, 345 GHz is used as the simulated frequency of observation for our analysis. Here, we will review the primary targets of the Event Horizon Telescope, and examine the dishes around the world capable of operating at the standards of the EHT.

1.2.1 Observation Targets

The Event Horizon Telescope’s angular resolution is sufficient for it to resolve event horizon-scale structure of the two supermassive black holes with the largest apparent size from Earth: Sagittarius A* (SgrA*) at the center of our galaxy, and Messier 87 (M87) in the Virgo constellation. The apparent horizons of these SgrA* and M87 are expected to be 52 microarcseconds [21] and 42 microarcseconds [1], respectively. These two primary targets each have unique scientific rewards for study and challenges for observation. SgrA* has an innermost stable circular orbital period between 4 minutes (for a maximal spin black hole) and half an hour (for a black hole with zero spin) [22]. Though this does not necessitate intense time variation at the angular scale at which the EHT observes, if it is present, the EHT would be able to observe multiple periods of this motion over the course of a night of observation, allowing for robust time domain studies on a short timescale.

Meanwhile, M87 has a very well-studied jet structure for which motion has been resolved on the timescale of weeks with observations at 7mm [52]. Shorter wavelength observations of the central region of M87 could link our understanding of the wider field-of-view jet dynamics of M87 to core processes. Indeed, the EHT has already resolved event horizon-scale structure at M87 [18]. As the array has grown and become more sensitive overall, so too have the opportunities for static imaging and time-domain studies of jet launching structures.

1.2.2 EHT Array Sites in 2018

As of the April 2018 observing campaign, the EHT has nine participating telescopes and arrays in its network, for which we will adopt a convenient acronym: the Atacama

Large (sub)-Millimeter Array, or ALMA, in Chile; the Atacama Pathfinder Experiment Telescope, or APEX, also in Chile and very close to ALMA; the Greenland Telescope, or GLT; the James Clark Maxwell Telescope, or JCMT, near the summit of Mauna Kea in Hawaii; the Large Millimeter Telescope, or LMT, in Mexico; the 30-meter telescope on Pico Veleta in Spain operated by the Institut de Radioastronomie Millimétrique, which we will refer to as PV; the Submillimeter Array, or SMA, located at the summit of Mauna Kea; the Submillimeter Telescope, or SMT, located on Mount Graham in Arizona; and finally, the South Pole Telescope, or SPT, operating at the National Science Foundation’s South Pole research station.

These stations span a large range of antenna separations. In the parlance of very-long-baseline interferometry, the EHT array has fairly comprehensive Fourier coverage of equatorial sources and thus has robust filling of the (u, v) plane - see Figure 1-1. The positions and sensitivities of the EHT sites in 2018 are tabulated in Table A.1. Note that the values for the system equivalent flux density (defined in Equation 2.1), which is inversely proportional to the sensitivity, are averages built from past measurements and are in practice measured during observation campaigns. In this thesis, these values are used for simulations, but our results are generally not sensitive to fluctuations in an individual SEFD by $\pm 50\%$.

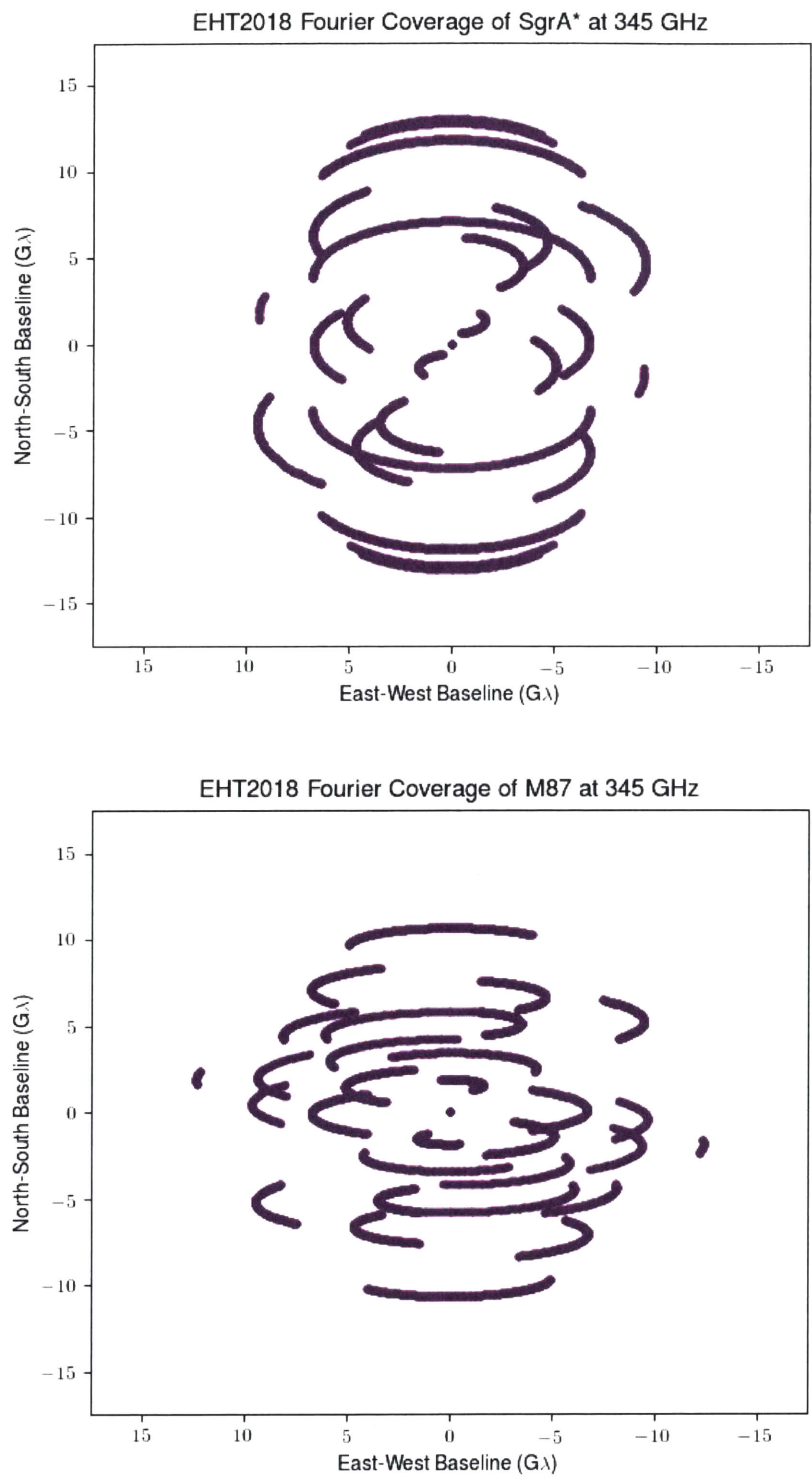


Figure 1-1: Fourier coverage of the EHT 2018 Array if observing at 345GHz.

Chapter 2

Motivation for Space Expansion of the Event Horizon Telescope

Orbiter very-long-baseline interferometry, or OVLBI, is an attractive idea - it removes fundamental limitations on baseline lengths that come from a fixed Earth radius, and ignores complications with atmospheric phase coherence as there is no atmosphere in the line of sight. That said, the parameter space of OVLBI is quite rich with considerations that must be made depending on the science goals of the project at hand. Here, we will examine the motivations for a particular type of space expansion to the Event Horizon Telescope, and simulate the benefits of such an expansion. By using EHT-standard algorithms [30] to reconstruct both images and movies of SgrA* and M87, we find that orbiters in low-medium Earth orbits enable short timescale imaging convergence - making movies of black holes.

2.1 Signal to Noise Ratio

A useful way to judge the sensitivity of a particular site is the system equivalent flux density, or SEFD. The SEFD is defined[51] as the flux density of a point source within the main beam required to generate a receiver noise power twice as large as the noise

power without a source. For an antenna with collecting area A :

$$\text{SEFD} = \frac{2kT_{\text{sys}}}{A}. \quad (2.1)$$

Here, k is the Boltzmann constant and T_{sys} is the system temperature of the receiver, a temperature associated with the power dissipated by an equivalent noiseless receiver attached to a matched resistive load. A larger, less noisy dish and receiver apparatus will be more sensitive and have a lower SEFD. For a single dish observing a source with flux density S , recording with a bandwidth $\Delta\nu$ and integration time τ ,

$$\text{SNR} = \frac{\eta_Q S \sqrt{2\Delta\nu\tau}}{\text{SEFD}}. \quad (2.2)$$

Intuitively, observing a wider bandwidth for more time will boost the SNR . Note the inclusion of the quantization efficiency factor η_Q . Some information is lost due to the discretization of the analog voltage readout from the receiver. For the two-bit quantization scheme of the Event Horizon Telescope backend, $\eta_Q \approx 0.86$. The SNR of the correlated output of two distant receivers (say, receivers 1 and 2) is the geometric mean of the SNR of the constituent signals:

$$\text{SNR}_{1,2} = \frac{\eta_Q S \sqrt{2\Delta\nu\tau}}{\sqrt{\text{SEFD}_1 \text{SEFD}_2}}. \quad (2.3)$$

The $\frac{1}{\sqrt{\text{SEFD}_1 \text{SEFD}_2}}$ dependence of the SNR means that, bandwidth and integration time being equal, an extremely sensitive station can give a fairly insensitive station seemingly disproportionate usefulness for VLBI. Looking back to Table A.1, we see that ALMA has an incredibly low SEFD, on the order of 100-200 Jy when operating at 345 GHz. Thus, a relatively tiny dish can form a baseline to ALMA that may have similar SNR to a baseline between two other, fairly sensitive ground sites.

2.2 Fourier Coverage

As we explored earlier, VLBI arrays measure the intensity distribution of a source by sampling spatial Fourier coefficients dependent on the length and orientation of antenna separations of the array. The Event Horizon Telescope makes use of Earth-rotation Fourier synthesis; as the Earth rotates, the vectors in the (u, v) plane separating the dishes in the array will rotate, sweeping out partial ellipses that slowly increment towards better knowledge of the source structure.

Orbiters, however, are not bound by the rotation rate of the Earth, and can thus form a significantly broader range of baselines to stations on the ground. In particular, the orientation and period of the orbit can be chosen to fill in gaps in the existing coverage of the array with far greater ease than is possible for a ground site, for which one must account for such factors as altitude, weather, and logistical serviceability when choosing where to construct a telescope or local array.

2.2.1 Orbit Design and Simulation

The goals of this proposed space expansion to the Event Horizon Telescope and previous OVLBI missions like VSOP and Spektr-R (and its upcoming follow-up, Spektr-M), differ in two primary regards. First, the mission-critical angular resolution of the EHT is not reliant on its baselines to space, as the Earth-sized ground-based array can already resolve the expected shadow dimensions of M87 and SgrA*. Second, as explained in our discussion of interferometric SNR in the age of ALMA, EHT space sites need not be antennas of comparable sensitivity to those on the ground.

Ideally, orbiting components of the EHT array would fill in gaps in existing coverage (Figure 1-1). Large regions of missing (u, v) coverage limit the field of view of reconstructed images [51], and filling gaps provides stronger confinement on the space of possible source intensity distributions that can explain a particular set of data. In particular, reducing the (u, v) separation between visibility measurements reduces the magnitude of sidelobes in the Fourier transform from visibility to the dirty image, making the application of any imaging algorithm easier and generically

reducing the error bars on imaging output.

A dish in low or medium Earth orbit satisfies these demands. In particular, when viewed from a distant source, an orbiter with low apogee distance will spend most of its orbit somewhere projected onto the face of the Earth, like any other EHT site. This geometric similarity guarantees that most of the baselines formed between ground sites and the orbiter will fall somewhere within the boundaries of existing EHT (u, v) coverage, thereby densely filling in gaps in visibility data.

It is worth noting that incremental changes to the orbiter apogee distance on the order of hundreds of kilometers do not have a great effect on the overall distribution of baselines formed to the orbiter, as such a change is a small fraction of the (X, Y, Z) position vector magnitude of the orbiter, and thus a small change in the (u, v) tracks. Assuming that the apogee distance is flexible, we are left with the challenge of selecting an appropriate orientation for the orbiter(s) to best enhance the EHT.

Other EHT collaborators have suggested a space expansion [41] involving two orbiters in offset orbits with space-space baselines designed to sweep through broad and regularly-spaced (u, v) coverage. We do not pursue this line of reasoning due to space-space baselines having very low SNR for small dishes, and due to the suggested orbital structure acquiring coverage on time scales too long for dynamical imaging.

For the purposes of this examination, we have selected the orbit of the International Space Station (or ISS) as a starting point for further optimization. This is a reasonable choice for several reasons: the ISS is a feasible location for a possible future radio dish; the ISS orbit is monitored closely to high precision, which is necessary for VLBI; finally, the orbit is mostly circular and lies close to the surface of the Earth, making it ideal for filling out the missing short and medium length baselines within EHT coverage. The ISS orbit has a period of approximately 1.5 hours.

To explore the parameter space of orbital orientation, we developed software to manipulate Two-Line Element sets (or TLEs) for use with EHT routines for observation simulation. This software allows us to create dummy TLEs for circular orbits in arbitrary orientations that are fully compatible with any Simplified Perturbation Model-based orbit calculator. Further, we can arbitrarily time-delay existing TLEs to

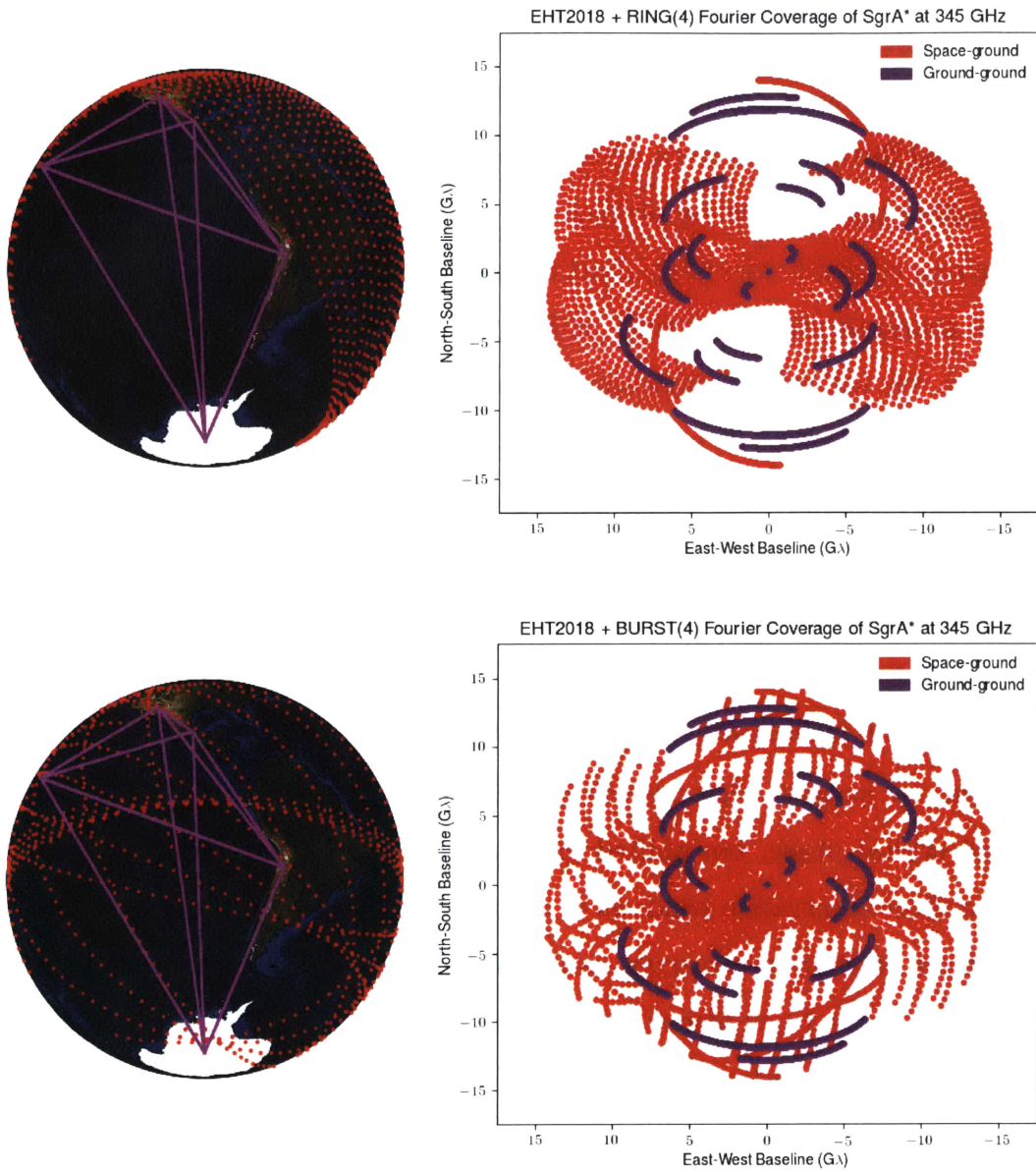


Figure 2-1: Example orbiter positions and (u, v) coverage of SgrA* with 4 orbiters. Positions are shown once per minute over six hours of observation starting at 0 GMST.

precisely shift orbital phase to any time relative to an EHT observation window. By rotating, time-delaying, and combining orbits of the ISS, dummy constellations of various orbiting configurations can be created and tested in EHT observation simulation environments.

It is not obvious how best to construct a constellation of orbiters for use with the EHT's existing ground sites. Imaging algorithms may benefit from different spatial and temporal distributions of (u, v) coverage. For example, consider two orbiters in circular orbits that completely overlap but are out of phase, such that the orbiters are always on opposite sides of the Earth. Baselines from the ground to these orbiters would be nearly identical over time, shifting only due to the rotations of the ground sites below. We will refer to this orbital paradigm of orbits with identical orientation but equally spaced phase as a 'ring' paradigm.

One might imagine that a ring paradigm might be ideal for smoothly gathering comprehensive visibility measurements over a long night of observation, with consistent spacing between data points and low variance in coverage over time. However, for a snapshot observation with duration on the order of an hour, such an orbiter spacing might be inefficient - some orbiters may never see the source.

Instead, we suggest what we will call the 'burst' paradigm: orbiters with synchronized orbital phase, but shifted in equal steps in angle. The burst paradigm allows for short observation windows to accrue robust Fourier coverage over the half-period of the orbiters in the array, as angularly spaced orbiters sweep out similarly spaced tracks in the (u, v) plane. However, even over longer observations, the Fourier coverage afforded by each paradigm can differ significantly.

A comparison of an example phase of these two paradigms can be found in Figure 2-1. Here, both paradigms have been assembled from four instances of the ISS orbit. The ring paradigm has been selected primarily to fill in absent horizontal coverage, while the burst paradigm fills in sparsely everywhere. In this orbital regime, the ring paradigm leaves no major gaps in (u, v) coverage in the regions spanned by its orbit, but it cannot simultaneously address all empty regions of EHT coverage at once. Meanwhile, the burst paradigm still leaves significant gaps between tracks.

Note that baselines between space dishes are not shown due to their very low SNR.

Testing various constellations of orbiters against the task of imaging reconstruction indicated that an array that was both rotated in orientation and time-delayed so that (u, v) coverage had low variance over time was most generally successful for any observation that lasted at least as long as one orbital period of the test orbiter. This paradigm yields the overall (u, v) coverage seen in the burst paradigm, but with a roughly constant number of ground-space baselines over time.

2.3 Imaging

The Event Horizon Telescope has many imaging techniques at its disposal, with varying strengths depending on source structure and observing array geometry. However, they can be broadly categorized as ‘static’ or ‘dynamical’ depending on whether they directly reconstruct single images or movies. Previous applications of standard EHT algorithms to archived VLBI data show that dynamical techniques may be necessary to accurately reconstruct images of time-varying sources.

For the purposes of our exploration of dynamical imaging, we rely on two packages recently developed by EHT collaborators: Starwarps [5] and Dynamical Imaging [30]. Each package takes an ordered list of initialization images, typically Gaussian intensity distributions centered on the sky position of the target, and fits a reconstructed image list to observed data (and, optionally, an image prior).

Imaging tests on synthetic data indicate that combined use of Starwarps and Dynamical Imaging produce movie reconstructions with greater consistency to the truth movie than either package imaging alone. Though both packages have significant customization capabilities that improve the imaging process depending on details of particular observations, we have taken a particular sequence of reconstruction and blurring steps as canonical so that output comparisons depend as entirely as possible on the arrays, and not on user fine-tuning. To that end, we examine simulated movies of the two primary targets of the EHT: SgrA* and M87.

The observing array used for these reconstructions is a combination of the ‘ring’

and ‘burst’ paradigms discussed in the previous section: four orbiters in rotated and time-delayed instances of the ISS orbit, aiming for a consistent number of space-ground baselines over time with a large overall (u, v) coverage. We generate synthetic observations assuming that each orbiter has a collecting surface with a diameter of 4 meters, and operates with $T_{\text{sys}} = 150$ K when observing at 345 GHz. Plugging in to Equation 2.1, we find an SEFD of approximately 47000 Jy. Finally, we assume that the entire array has absolute phase-referencing at every site, allowing image reconstructions to be performed with complex visibilities.

2.3.1 Imaging SgrA*

The black hole candidate at the center of the Milky Way, Sagittarius A*, is the primary observational target of the Event Horizon Telescope. Its large apparent size and previously observed flaring structure [19] make it a valuable target for explorations of general relativistic behavior near the event horizon. Reconstructing static images of SgrA* at the event horizon scale is a significant imaging challenge, and the focus of much of EHT imaging algorithm development. However, SgrA* is expected to evolve rapidly in time, with an innermost stable circular orbital timescale of less than half an hour, requiring the EHT’s novel dynamical imaging techniques to reconstruct motion on timescales shorter than typical EHT observations.

To test and compare the capabilities of the observation and imaging pipeline of the EHT and various configurations of a space-enabled EHT, we simulate observations of static and dynamic images of SgrA* at 345 GHz. The static image is of a crescent model [6] that is broadly consistent with past EHT observations of SgrA*, while the time-evolving simulation models an orbiting hot spot [7]. We find that the addition of 4×4 m diameter dishes makes the difference between success and failure in reconstructing images and movies of SgrA* on very short observational timescales, as in Figure 2-2.

The disproportionate utility of space dishes becomes even more clear when compared with a hypothetical future EHT with small dishes added on the ground. We simulate four four-meter-diameter dishes at four planned EHT locations: Kitt Peak,

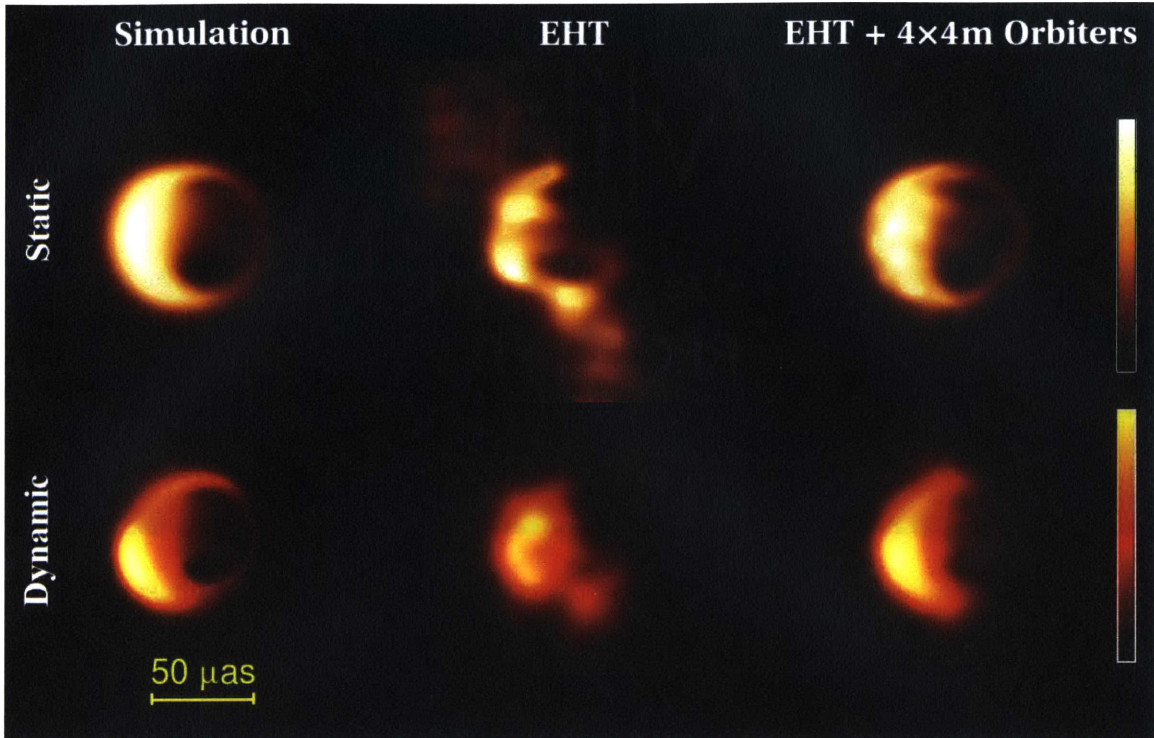


Figure 2-2: Simulated static and dynamical imaging of 2 hour observations of SgrA* with phase-coherent EHT and space dishes at .87 mm. A 16 GHz bandwidth and 30 second integration time are assumed for each individual observation, advancing 30 seconds between observations. The first row are reconstructions of a static crescent; the second are frames from movies of an orbiting "hot spot" model of SgrA* with a period of 30 minutes.

in Arizona; the Inyo Mountains, in California; the Plateau de Bure, in the French Alps; and Gamsberg, Namibia. Despite these additions, the ground-based EHT leaves significant erroneous flux outside of the hotspot, while the space-enabled EHT reconstructs the image almost perfectly, as in Figure 2-3.

2.3.2 Imaging M87

Dense Fourier coverage on short timescales provides imaging benefits on sources with slow time-variation as well. 7mm observations of M87 have resolved jet motion on timescales of weeks [52], while the EHT has resolved structure on the scale of the black hole shadow [1, 18]. Successful dynamical reconstruction of motion in the central emitting region may connect core dynamics to other observations of jet motion,

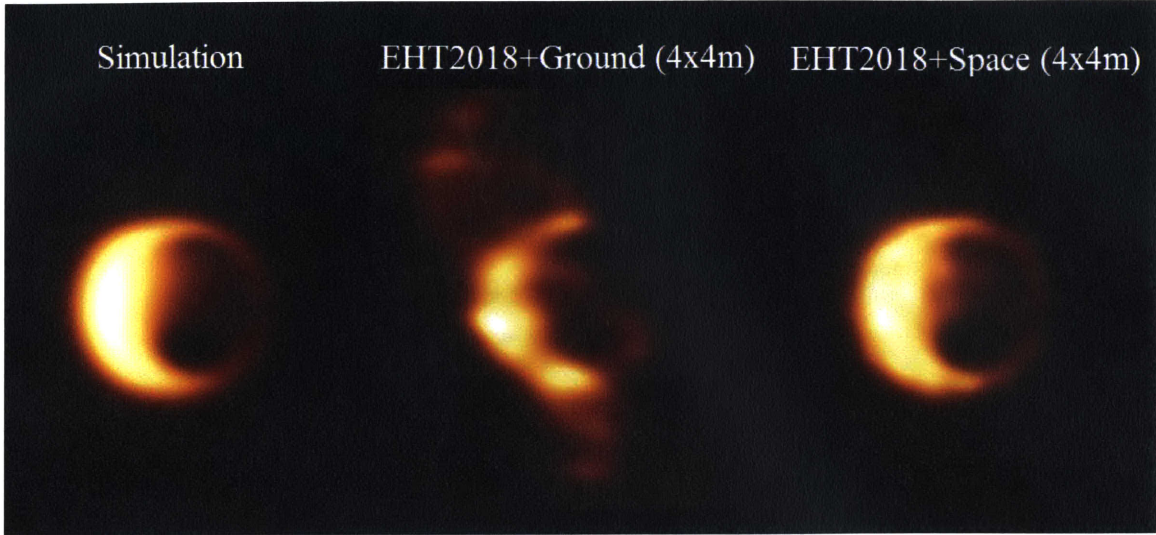


Figure 2-3: Simulated static of 90 minute observations of SgrA* with phase-coherent ground-enhanced EHT and space dishes at .87 mm. A 16 GHz bandwidth and 30 second integration time are assumed for each individual observation, advancing 30 seconds between observations.

elucidating whether the jet is powered by gravitational energy from accreted material [3], or by the spin of the black hole itself [4].

The comprehensive Fourier coverage provided by a constellation of orbiting dishes allows for robust observations of any target on fairly short timescales. For M87, this allows lengthy monitoring to be assembled from very brief observations once per night, or even once per week. We find that nightly one and a half hour observations of a simulated jet emission from M87 [38] are sufficient to assemble high quality dynamical reconstructions with space dishes, whereas observations with the 2018 EHT do not lead to convergent reconstructions of high quality Figure 2-4. Short observation schedules allow for efficient use of expensive ground telescope time, and free up orbiting dishes for other targets.

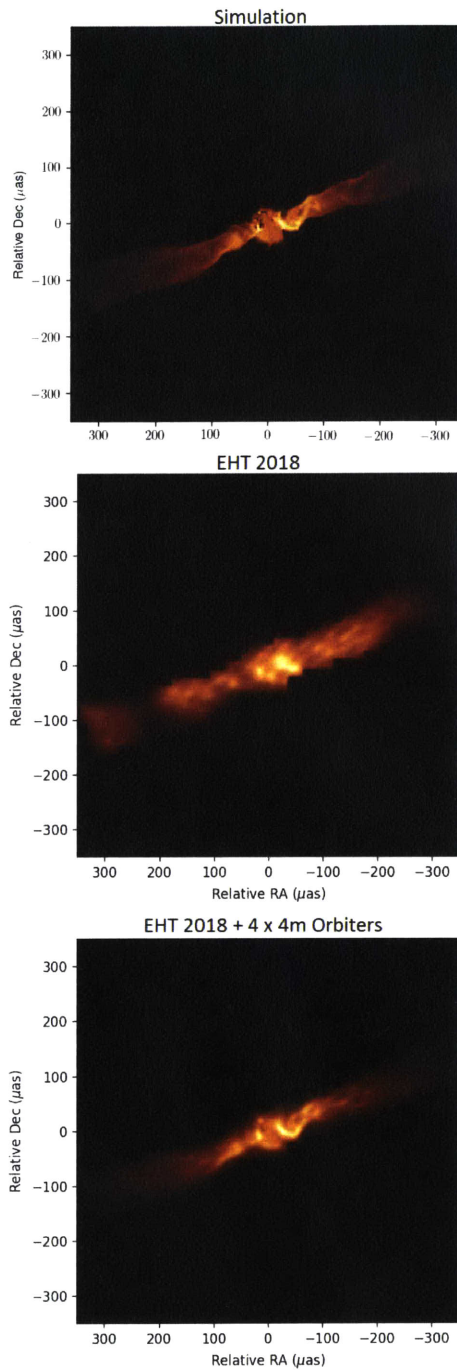


Figure 2-4: Single frames from dynamical reconstructions of 3-hour synthetic observations of simulated M87 jet motion. A mask composed of all non-zero values in the simulation has been applied to the fit space in the reconstructions. At top, the input video. At center, reconstructing from observations with the EHT2018. At bottom, the EHT2018 + 4x4m orbiting dishes. The addition of orbiting dishes allows the correct reconstruction of outflow structures and eliminates most of the erroneous rippling structure in the synthetic EHT2018 simulation.

Chapter 3

Numerical Constraints on Space-Based Observation

The technical requirements of operating an orbiting station as part of a VLBI network place constraints on the basic parameters of observation. By demanding that orbiters function at the full 16 GHz bandwidth of the EHT, we can place constraints on other aspects of the dishes, ultimately finding need for technological development to enable OVLBI at high frequencies.

3.1 Integration Time

The integration time τ is the length of time over which visibility measurements are binned together during data reduction. The integration time is limited by the time scale of phase coherence, which may be reduced by turbulence in the atmosphere. However, there are specific constraints on the integration time that come from the geometry and hardware of the orbiter, and we will focus on those demands here.

3.1.1 SNR and Noise on Strong Baselines

The proposed space expansions to the EHT leverage the fact that baselines from ALMA to space sites will benefit from ALMA's incredibly high sensitivity, allowing

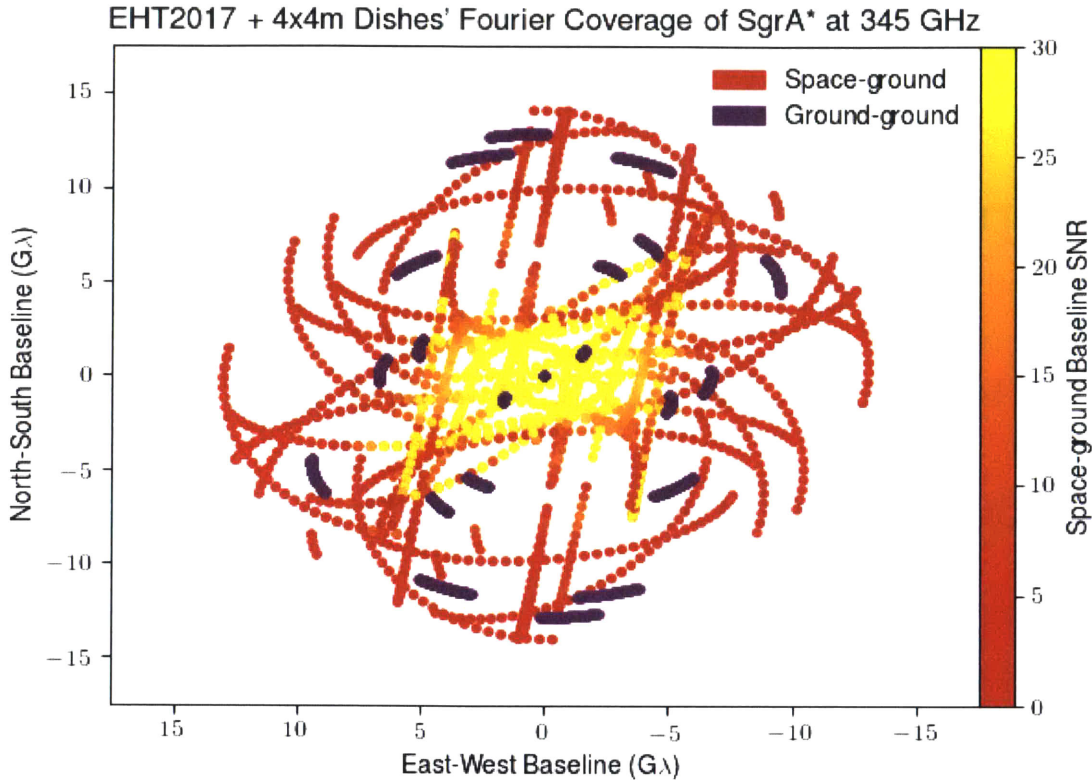


Figure 3-1: Fourier coverage over 1.5 hours of a simulated hotspot[7] of SgrA* at .87 mm by the EHT 2018 array when four, four-meter dishes in low Earth orbit are added to the array, viewed after accounting for the ensemble-average blurring by the scattering kernel towards SgrA*. Ground-ground baselines are shown in purple, while space-ground baselines are shown in the orange gradient, scaling with SNR.

smaller, otherwise unsuitable dish sizes to be used in space. In Chapter 2, a dynamical reconstruction of a hotspot around SgrA* was built from a two-hour observation conducted with the 2018 EHT array along with four orbiters with 4 m diameter collecting surfaces. This observation assumed the full 16 GHz bandwidth of the EHT and an integration time of 30 seconds, which is known to be well within coherence for sensitive ground sites like ALMA. An SNR-sensitive plot of the the (u, v) coverage associated with this observation is shown in Figure 3-1.

As we see in the figure, baselines to this set of orbiters have detectable SNR out to long baselines, especially for ALMA-space baselines. However, the SNR is affected by source structure, which in this case is governed by the hotspot simulation.

We can apply the same logic while maintaining source-agnosticism by recasting the interferometric SNR (Equation 2.3) in terms of the thermal noise on a baseline:

$$\text{SNR}_{1,2} = \frac{S}{\sigma} \quad (3.1)$$

We can now parametrize the quality of a particular baseline observing with a given bandwidth $\Delta\nu$ and constituent system equivalent flux densities by the tuning of a single parameter - the integration time τ . More concretely, we find the thermal noise σ to be

$$\sigma = \frac{1}{\eta_Q} \sqrt{\frac{\text{SEFD}_1 \text{SEFD}_2}{2\Delta\nu\tau}}. \quad (3.2)$$

As baselines from ALMA to orbiting dishes form the backbone of a potential expansion of the EHT to space, it is reasonable to demand that baselines from ALMA to each dish are comparable to existing baselines. Using our previously computed and tabulated values for the SEFDs of ALMA and our test orbiter (150 Jy and 47000 Jy, respectively), we can compute a minimum integration time τ_{min} based on an existing average thermal noise, σ_{avg} :

$$\tau_{min} = \frac{\text{SEFD}_1 \text{SEFD}_2}{2\Delta\nu} \left(\frac{1}{\eta_Q \sigma_{avg}} \right)^2. \quad (3.3)$$

Simulations with the 2018 EHT array show a mean thermal noise on intensity measurements of $\sigma_{avg} \approx .005$ Jy, yielding $\tau_{min} \approx 12$ seconds. This is a soft lower bound, as baselines to space need not be strictly better than average ground baselines.

3.1.2 Motion Blurring

Though the motion of VLBI observing sites is crucial to Fourier synthesis, it also introduces fundamental limitations on integration. As the baseline vector \vec{u} rotates, the visibility measurement associated with that interferometric baseline is blurred. Thompson, Moran, and Swanson provide a bounding condition on Earth site integration time to ensure robust operation[51]:

$$\tau < \frac{1}{\omega_E D_\lambda \theta_f} \quad (3.4)$$

Here, ω_E is the rotation rate of the Earth, $D_\lambda = |\vec{u}_{max}|$ is the length of the largest baseline in wavelengths, and θ_f is the field of view to be imaged. The factor of $\omega_E D_\lambda$ is the length of the arc traced in the (u, v) plane per second; we can create a new relation by simply changing the rotation rate to that of our orbiter, $\frac{2\pi}{P}$, for a period $P \approx 1.5$ hours. Assuming we are interested only in filling in gaps in existing (u, v) coverage, we only care about coherent averaging measurements out to the maximum baseline of the existing array, so $D_\lambda \approx 10 G\lambda$. These values altogether yield $\tau < 1$ minute. Thompson, Moran, and Swanson recommend an integration time of at most half of this upper bound, limiting us to 30 seconds, as used in the simulations in Chapter 2.

3.2 Hardware Specifications

Beyond constraints on the integration time, putting ultra-high frequency VLBI equipment into space comes with a number of miscellaneous hardware requirements that will shape the technological research required in the next decade to make it a reality. We examine some of these constraints here.

3.2.1 Local Oscillators

VLBI requires that every station in the array have a very precise and stable frequency standard in order to measure the phase information of the receiver signal. The current standard in high frequency VLBI that is used by virtually all EHT sites is the hydrogen maser. Though the Spektr-R mission successfully performed OVLBI with two on-board hydrogen masers[20], it is not clear that a maser would fit on a smaller orbiter such as those proposed by this thesis. Recent research indicates that smaller crystal oscillators[17] may soon rival the performance of hydrogen masers, allowing a lighter payload to orbit with the same phase stability.

3.2.2 Antenna Surface

The simulations conducted for this investigation have so far computed system-equivalent flux densities for simulated sites from an assumed collecting area A computed geometrically from a dish diameter d . However, in reality, collecting surfaces are imperfect, and carry a surface deviation[51] σ indicating the position uncertainty of the material of the antenna in the axis normal to the ideal shape. This leads to an effective area A that is distinct from the geometric area A_0 , as given by the Ruze formula:

$$\frac{A}{A_0} = \exp -\left(\frac{4\pi\sigma}{\lambda}\right)^2. \quad (3.5)$$

The efficiency of a collecting surface is thus driven by the ratio $\frac{\sigma}{\lambda}$. For observations at .87 mm and 1.3 mm, we show the efficiency curves in Figure 3-2. Ideally, a dish receiving at .87 mm would have a surface accuracy of less than 20 microns in order to have an efficiency close to 1, but this is difficult to attain.

Space dishes are particularly troubled by surface considerations due to the deformations caused by transit to space, and the difficulty of creating deployable surfaces that maintain a low surface deviation. The now-defunct VSOP-2 mission called for a large deployable reflector made from gold-plated molybdenum mesh, but tests indicated that it would not perform well at high frequencies[31], and that the deployable mesh paradigm would not generalize to wavelengths shorter than centimeter-scale. However, non-deployable architectures such as a fixed carbon-fiber mold, can attain significantly higher surface accuracies[15] at the cost of needing to fit into the fairing of a delivery vehicle.

The four-meter-diameter dishes suggested by this thesis would fit into the quoted fairing of the SpaceX Falcon 9 rocket. For a constellation of dishes, an ideal launch architecture would involve a stack of these dishes released in different directions at the appropriate altitude. That said, astrodynamical launch considerations are beyond the scope of this thesis.

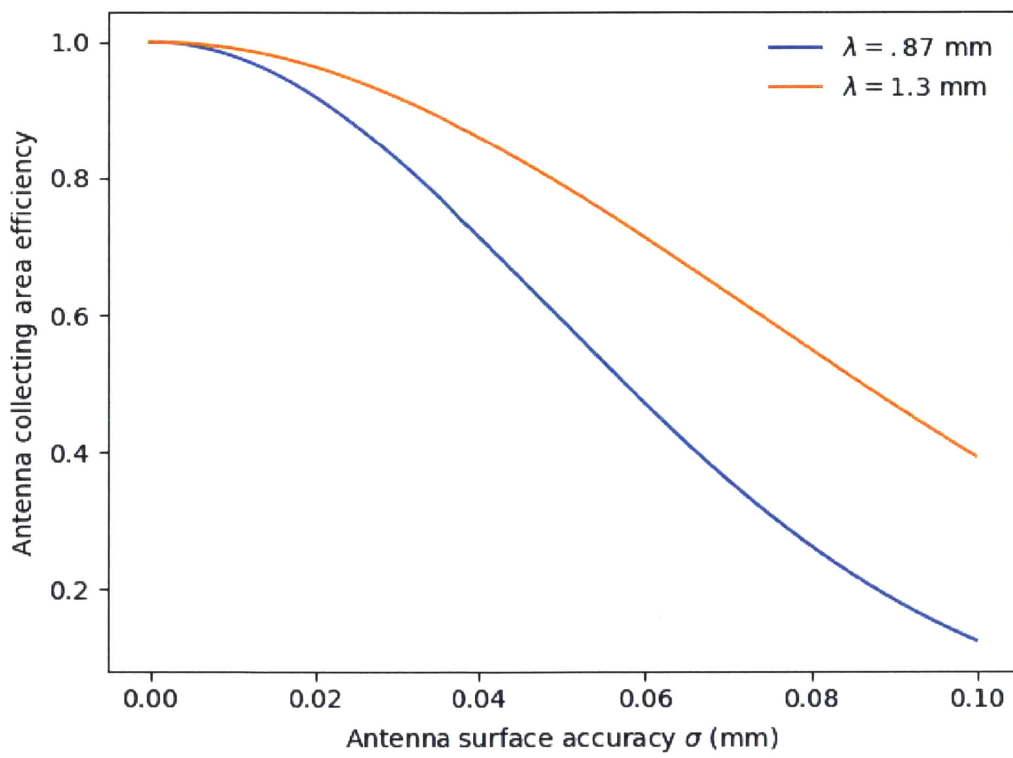


Figure 3-2: Ruze formula plotted for observation at .87 mm (lower curve) and 1.3 mm (higher curve).

Chapter 4

Conclusion and Paths Forward

By simulating orbiting VLBI stations in the Event Horizon Telescope and generating synthetic observations for use with EHT-standard imaging processes, we have demonstrated that small orbiters are disproportionately useful for increasing image quality, and may be a promising path of growth for the EHT array over the next decade, enabling the reconstruction of movies of black holes.

However, this thesis presents only initial considerations before expanding the Event Horizon Telescope to space. The real feasibility of such an undertaking will depend on advances in the technologies detailed in Chapter 3, as well as on new understanding of SgrA* and M87 that will be gained from analysis of existing EHT data. Characterizing the structure and time-variability of SgrA* will allow more decisive orbital construction to address the needs of the array.

Advances in imaging algorithms may also change the exact demands on OVLBI with the EHT. As we saw in Chapter 2, low and medium Earth orbiters tend to form dense coverage on short and medium baselines, but the distance between measurements in individual tracks through the (u, v) plane is significantly higher than for ground sites due to the higher angular speed of the orbiter. Though this blurring is already accounted for in limitations to the integration time as discussed in Chapter 3, it is conceivable that slower, more eccentric orbits with high apogee oriented towards SgrA* may be better for imaging. Comprehensive numerical tests over a larger space of orbits are a promising next step.

Meanwhile, as these parallel courses move forward towards making a new OVLBI mission a reality, the Event Horizon Telescope is maturing as a ground based array. We have a growing arsenal of hardware and analytical tools to observe the structure in the immediate vicinity of a black hole event horizon, and the lessons learned from these observations will inform and enable VLBI for decades to come.

Appendix A

EHT Station Parameters

The EHT collaboration maintains measurements of the sensitivities of the dishes in the array. Further, for some telescopes with planned upgrades to operation at 345 GHz, the SEFD can be predicted rather than measured. For the 2018 array, those values are below. SEFDs are in Jy, distances are in m.

Table A.1: Estimated EHT Station Parameters in 2018.

Facility	Diameter	SEFD _{1.3mm}	SEFD _{0.87mm}	X	Y	Z
JCMT	15	6000	8000	-5464584.68	-2493001.17	2150653.98
SMA	7 × 6 m	4900	7400	-5464555.49	-2492927.99	2150797.18
SMT	10	5000	7500	-1828796.2	-5054406.8	3427865.2
APEX	12	3500	6000	2225039.53	-5441197.63	-2479303.36
ALMA	~ 40 × 12 m	90	150	2225061.164	-5440057.37	-2481681.15
SPT	10	5000	8000	0.01	0.01	-6359609.7
LMT	50	600	1400	-768715.63	-5988507.07	2063354.85
PV	30	1400	2800	5088967.75	-301681.186	3825012.206

Bibliography

- [1] K. Akiyama, R.-S. Lu, V. L. Fish, S. S. Doeleman, A. E. Broderick, J. Dexter, K. Hada, M. Kino, H. Nagai, M. Honma, M. D. Johnson, J. C. Algaba, K. Asada, C. Brinkerink, R. Blundell, G. C. Bower, R. Cappallo, G. B. Crew, M. Dexter, S. A. Dzib, R. Freund, P. Friberg, M. Gurwell, P. T. P. Ho, M. Inoue, T. P. Krichbaum, L. Loinard, D. MacMahon, D. P. Marrone, J. M. Moran, M. Nakamura, N. M. Nagar, G. Ortiz-Leon, R. Plambeck, N. Pradel, R. A. Primiani, A. E. E. Rogers, A. L. Roy, J. SooHoo, J.-L. Tavares, R. P. J. Tilanus, M. Titus, J. Wagner, J. Weintroub, P. Yamaguchi, K. H. Young, A. Zensus, and L. M. Zzurys. 230 GHz VLBI Observations of M87: Event-horizon-scale Structure during an Enhanced Very-high-energy γ -Ray State in 2012. *ApJ*, 807:150, July 2015.
- [2] J. W. M. Baars, J. F. van der Brugge, J. L. Casse, J. P. Hamaker, L. H. Sondaar, J. J. Visser, and K. J. Wellington. The synthesis radio telescope at Westerbork. *IEEE Proceedings*, 61:1258–1266, September 1973.
- [3] R. D. Blandford and D. G. Payne. Hydromagnetic flows from accretion discs and the production of radio jets. *MNRAS*, 199:883–903, June 1982.
- [4] R. D. Blandford and R. L. Znajek. Electromagnetic extraction of energy from Kerr black holes. *MNRAS*, 179:433–456, May 1977.
- [5] K. L. Bouman, M. D. Johnson, A. V. Dalca, A. A. Chael, F. Roelofs, S. S. Doeleman, and W. T. Freeman. Reconstructing Video from Interferometric Measurements of Time-Varying Sources. *ArXiv e-prints*, November 2017.
- [6] A. E. Broderick, V. L. Fish, M. D. Johnson, K. Rosenfeld, C. Wang, S. S. Doeleman, K. Akiyama, T. Johannsen, and A. L. Roy. Modeling Seven Years of Event Horizon Telescope Observations with Radiatively Inefficient Accretion Flow Models. *ApJ*, 820:137, April 2016.
- [7] A. E. Broderick and A. Loeb. Imaging optically-thin hotspots near the black hole horizon of Sgr A* at radio and near-infrared wavelengths. *MNRAS*, 367:905–916, April 2006.
- [8] N. W. Broten, T. H. Legg, J. L. Locke, C. W. McLeish, R. S. Richards, R. M. Chisholm, H. P. Gush, J. L. Yen, and J. A. Galt. Long Base Line Interferometry: A New Technique. *Science*, 156:1592–1593, June 1967.

- [9] N. W. Broten, J. L. Locke, T. H. Legg, C. W. McLeish, and R. S. Richards. Observations of Quasars using Interferometer Baselines up to 3,074 km. *Nature*, 215:38, July 1967.
- [10] G. W. Brown, T. D. Carr, and W. F. Block. Long-Baseline Interferometry of S-Bursts from Jupiter. *Astrophysics Letters*, 1:89, 1968.
- [11] R. H. Brown and R. G. Twiss. A New type of interferometer for use in radio astronomy. *Philosophical Magazine*, 45:663–682, March 1954.
- [12] A. A. Chael, M. D. Johnson, K. L. Bouman, L. L. Blackburn, K. Akiyama, and R. Narayan. Interferometric Imaging Directly with Closure Phases and Closure Amplitudes. *ApJ*, 857:23, April 2018.
- [13] A. A. Chael, M. D. Johnson, R. Narayan, S. S. Doeleman, J. F. C. Wardle, and K. L. Bouman. High-resolution Linear Polarimetric Imaging for the Event Horizon Telescope. *ApJ*, 829:11, September 2016.
- [14] W. N. Christiansen and J. A. Warburton. The Distribution of Radio Brightness over the Solar Disk at a Wavelength of 21 Centimetres. III. The Quiet Sun—Two-Dimensional Observations. *Australian Journal of Physics*, 8:474, December 1955.
- [15] L. Datashvili, N. Maghaldadze, S. Endler, J. Pauw, P. He, H. Baier, A. Ihle, and J. Santiago Prowlad. Advances in Mechanical Architectures of Large Precision Space Apertures. In *13th European Conference on Spacecraft Structures, Materials and Environmental Testing*, volume 727 of *ESA Special Publication*, page 175, June 2014.
- [16] S. Dibi, S. Markoff, R. Belmont, J. Malzac, N. M. Barrière, and J. A. Tomsick. Exploring plasma evolution during Sagittarius A* flares. *MNRAS*, 441:1005–1016, June 2014.
- [17] S. Doeleman, T. Mai, A. E. E. Rogers, J. G. Hartnett, M. E. Tobar, and N. Nand. Adapting a Cryogenic Sapphire Oscillator for Very Long Baseline Interferometry. *PASP*, 123:582, May 2011.
- [18] S. S. Doeleman, V. L. Fish, D. E. Schenck, C. Beaudoin, R. Blundell, G. C. Bower, A. E. Broderick, R. Chamberlin, R. Freund, P. Friberg, M. A. Gurwell, P. T. P. Ho, M. Honma, M. Inoue, T. P. Krichbaum, J. Lamb, A. Loeb, C. Lonsdale, D. P. Marrone, J. M. Moran, T. Oyama, R. Plambeck, R. A. Primiani, A. E. E. Rogers, D. L. Smythe, J. SooHoo, P. Strittmatter, R. P. J. Tilanus, M. Titus, J. Weintroub, M. Wright, K. H. Young, and L. M. Ziurys. Jet-Launching Structure Resolved Near the Supermassive Black Hole in M87. *Science*, 338:355, October 2012.
- [19] S. S. Doeleman, J. Weintroub, A. E. E. Rogers, R. Plambeck, R. Freund, R. P. J. Tilanus, P. Friberg, L. M. Ziurys, J. M. Moran, B. Corey, K. H. Young, D. L.

- Smythe, M. Titus, D. P. Marrone, R. J. Cappallo, D. C.-J. Bock, G. C. Bower, R. Chamberlin, G. R. Davis, T. P. Krichbaum, J. Lamb, H. Maness, A. E. Niell, A. Roy, P. Strittmatter, D. Werthimer, A. R. Whitney, and D. Woody. Event-horizon-scale structure in the supermassive black hole candidate at the Galactic Centre. *Nature*, 455:78–80, September 2008.
- [20] D. A. Duev, M. V. Zakhvatkin, V. A. Stepanyants, G. Molera Calvés, S. V. Pogrebenko, L. I. Gurvits, G. Cimò, and T. M. Bocanegra Bahamón. RadioAstron as a target and as an instrument: Enhancing the Space VLBI mission’s scientific output. *A&A*, 573:A99, January 2015.
- [21] V. L. Fish, S. S. Doeleman, C. Beaudoin, R. Blundell, D. E. Bolin, G. C. Bower, R. Chamberlin, R. Freund, P. Friberg, M. A. Gurwell, M. Honma, M. Inoue, T. P. Krichbaum, J. Lamb, D. P. Marrone, J. M. Moran, T. Oyama, R. Plambeck, R. Primiani, A. E. E. Rogers, D. L. Smythe, J. SooHoo, P. Strittmatter, R. P. J. Tilanus, M. Titus, J. Weintraub, M. Wright, D. Woody, K. H. Young, and L. M. Ziurys. 1.3 mm Wavelength VLBI of Sagittarius A*: Detection of Time-variable Emission on Event Horizon Scales. *ApJL*, 727:L36, February 2011.
- [22] V. P. Frolov and I. D. Novikov. *Black hole physics : basic concepts and new developments*. 1998.
- [23] A. M. Ghez, S. Salim, N. N. Weinberg, J. R. Lu, T. Do, J. K. Dunn, K. Matthews, M. R. Morris, S. Yelda, E. E. Becklin, T. Kremenek, M. Milosavljevic, and J. Naiman. Measuring Distance and Properties of the Milky Way’s Central Supermassive Black Hole with Stellar Orbits. *ApJ*, 689:1044–1062, December 2008.
- [24] H. Hirabayashi, H. Hirose, H. Kobayashi, Y. Murata, P. G. Edwards, E. B. Fomalont, K. Fujisawa, T. Ichikawa, T. Kii, J. E. J. Lovell, G. A. Moellenbrock, R. Okayasu, M. Inoue, N. Kawaguchi, S. Kamenoi, K. M. Shibata, Y. Asaki, T. Bushimata, S. Enome, S. Horiuchi, T. Miyaji, T. Umemoto, V. Migenes, K. Wajima, J. Nakajima, M. Morimoto, J. Ellis, D. L. Meier, D. W. Murphy, R. A. Preston, J. G. Smith, S. J. Tingay, D. L. Traub, R. D. Wietfeldt, J. M. Benson, M. J. Claussen, C. Flatters, J. D. Romney, J. S. Ulvestad, L. R. D’Addario, G. I. Langston, A. H. Minter, B. R. Carlson, P. E. Dewdney, D. L. Jauncey, J. E. Reynolds, A. R. Taylor, P. M. McCulloch, W. H. Cannon, L. I. Gurvits, A. J. Mioduszewski, R. T. Schilizzi, and R. S. Booth. Overview and Initial Results of the Very Long Baseline Interferometry Space Observatory Programme. *Science*, 281:1825, September 1998.
- [25] D. E. Hogg, G. H. MacDonald, R. G. Conway, and C. M. Wade. Synthesis of Brightness Distribution in Radio Sources. *AJ*, 74:1206–1213, December 1969.
- [26] R. C. Jennison. A phase sensitive interferometer technique for the measurement of the Fourier transforms of spatial brightness distributions of small angular extent. *MNRAS*, 118:276, 1958.

- [27] R. C. Jennison and M. K. Das Gupta. Fine Structure of the Extra-terrestrial Radio Source Cygnus I. *Nature*, 172:996–997, November 1953.
- [28] R. C. Jennison and M. K. D. Gupta. V. The measurement of the angular diameter of two intense radio sources. I: A radio interferometer using post-detector correlation. *Philosophical Magazine*, 1:55–64, January 1956.
- [29] R. C. Jennison and V. Latham. The brightness distribution within the radio sources Cygnus A (19N4A) and Cassiopeia A (23N5A). *MNRAS*, 119:174, 1959.
- [30] M. D. Johnson, K. L. Bouman, L. Blackburn, A. A. Chael, J. Rosen, H. Shiokawa, F. Roelofs, K. Akiyama, V. L. Fish, and S. S. Doeleman. Dynamical Imaging with Interferometry. *ApJ*, 850:172, December 2017.
- [31] K. Kamegai and M. Tsuboi. Measurements of an Antenna Surface for a Millimeter-Wave Space Radio Telescope. II. Metal Mesh Surface for Large Deployable Reflector. *PASJ*, 65:21, February 2013.
- [32] N. S. Kardashev, V. V. Khartov, V. V. Abramov, V. Y. Avdeev, A. V. Alakoz, Y. A. Aleksandrov, S. Ananthakrishnan, V. V. Andreyanov, A. S. Andrianov, N. M. Antonov, M. I. Artyukhov, M. Y. Arkhipov, W. Baan, N. G. Babakin, V. E. Babyshkin, N. Bartel', K. G. Belousov, A. A. Belyaev, J. J. Berulis, B. F. Burke, A. V. Biryukov, A. E. Bubnov, M. S. Burgin, G. Busca, A. A. Bykadorov, V. S. Bychkova, V. I. Vasil'kov, K. J. Wellington, I. S. Vinogradov, R. Wietfeldt, P. A. Voitsik, A. S. Gvamichava, I. A. Girin, L. I. Gurvits, R. D. Dagkesamanskii, L. D'Addario, G. Giovannini, D. L. Jauncey, P. E. Dewdney, A. A. D'yakov, V. E. Zharov, V. I. Zhuravlev, G. S. Zaslavskii, M. V. Zakhvatkin, A. N. Zinov'ev, Y. Ilinen, A. V. Ipatov, B. Z. Kanevskii, I. A. Knorin, J. L. Casse, K. I. Kellermann, Y. A. Kovalev, Y. Y. Kovalev, A. V. Kovalenko, B. L. Kogan, R. V. Komaev, A. A. Konovalenko, G. D. Kopelyanskii, Y. A. Korneev, V. I. Kostenko, A. N. Kotik, B. B. Kreisman, A. Y. Kukushkin, V. F. Kulishenko, D. N. Cooper, A. M. Kut'kin, W. H. Cannon, M. G. Larionov, M. M. Lisakov, L. N. Litvinenko, S. F. Likhachev, L. N. Likhacheva, A. P. Lobanov, S. V. Logvinenko, G. Langston, K. McCracken, S. Y. Medvedev, M. V. Melekhin, A. V. Menderov, D. W. Murphy, T. A. Mizyakina, Y. V. Mozgovi, N. Y. Nikolaev, B. S. Novikov, I. D. Novikov, V. V. Oreshko, Y. K. Pavlenko, I. N. Pashchenko, Y. N. Ponomarev, M. V. Popov, A. Pravin-Kumar, R. A. Preston, V. N. Pyshnov, I. A. Rakhimov, V. M. Rozhkov, J. D. Romney, P. Rocha, V. A. Rudakov, A. Räisänen, S. V. Sazankov, B. A. Sakharov, S. K. Semenov, V. A. Serebrennikov, R. T. Schilizzi, D. P. Skulachev, V. I. Slysh, A. I. Smirnov, J. G. Smith, V. A. Soglasnov, K. V. Sokolovskii, L. H. Sondaar, V. A. Stepan'yants, M. S. Turygin, S. Y. Turygin, A. G. Tuchin, S. Urpo, S. D. Fedorchuk, A. M. Finkel'shtein, E. B. Fomalont, I. Fejes, A. N. Fomina, Y. B. Khapin, G. S. Tsarevskii, J. A. Zensus, A. A. Chuprikov, M. V. Shatskaya, N. Y. Shapirovskaya, A. I. Sheikhet, A. E. Shirshakov, A. Schmidt, L. A. Shnyreva, V. V. Shpilevskii, R. D. Ekers, and

- V. E. Yakimov. “RadioAstron”—A telescope with a size of 300 000 km: Main parameters and first observational results. *Astronomy Reports*, 57:153–194, March 2013.
- [33] G. S. Levy, R. P. Linfield, C. D. Edwards, J. S. Ulvestad, J. F. Jordan, Jr., S. J. Dinardo, C. S. Christensen, R. A. Preston, L. J. Skjerve, L. R. Stavert, B. F. Burke, A. R. Whitney, R. J. Cappallo, A. E. E. Rogers, K. B. Blaney, M. J. Maher, C. H. Ottenhoff, D. L. Jauncey, W. L. Peters, J. Reynolds, T. Nishimura, T. Hayashi, T. Takano, T. Yamada, H. Hirabayashi, M. Morimoto, M. Inoue, T. Shiomi, N. Kawaguchi, H. Kunimori, M. Tokumaru, and F. Takahashi. VLBI using a telescope in Earth orbit. I - The observations. *ApJ*, 336:1098–1104, January 1989.
- [34] L. D. Matthews, G. B. Crew, S. S. Doeleman, R. Lacasse, A. F. Saez, W. Alef, K. Akiyama, R. Amestica, J. M. Anderson, D. A. Barkats, A. Baudry, D. Broguière, R. Escoffier, V. L. Fish, J. Greenberg, M. H. Hecht, R. Hiriart, A. Hirota, M. Honma, P. T. P. Ho, C. M. V. Impellizzeri, M. Inoue, Y. Kohno, B. Lopez, I. Martí-Vidal, H. Messias, Z. Meyer-Zhao, M. Mora-Klein, N. M. Nagar, H. Nishioka, T. Oyama, V. Pankratius, J. Perez, N. Phillips, N. Pradel, H. Rottmann, A. L. Roy, C. A. Ruszczyk, B. Shillue, S. Suzuki, and R. Treacy. The ALMA Phasing System: A Beamforming Capability for Ultra-high-resolution Science at (Sub)Millimeter Wavelengths. *PASP*, 130(1):015002, January 2018.
- [35] L. L. McCready, J. L. Pawsey, and R. Payne-Scott. Solar Radiation at Radio Frequencies and Its Relation to Sunspots. *Proceedings of the Royal Society of London Series A*, 190:357–375, August 1947.
- [36] A. A. Michelson. On the Application of Interference Methods to Astronomical Measurements. *ApJ*, 51:257, June 1920.
- [37] B. Y. Mills. The Radio Brightness Distributions over Four Discrete Sources of Cosmic Noise. *Australian Journal of Physics*, 6:452, December 1953.
- [38] M. Mościbrodzka, H. Falcke, and H. Shiokawa. General relativistic magnetohydrodynamical simulations of the jet in M 87. *A&A*, 586:A38, February 2016.
- [39] P. A. O’Brien. The distribution of radiation across the solar disk at metre wavelength. *MNRAS*, 113:597, 1953.
- [40] D. Palumbo, S. Doeleman, M. Johnson, K. Bouman, and A. Chael. Making movies of black holes: Simulated orbiting dishes and technical challenges. in prep.
- [41] F. et al Roelofs. Imaging the event horizon of sagittarius a* from space. in prep.
- [42] B. Rowson. High resolution observations with a tracking radio interferometer. *MNRAS*, 125:177, 1963.

- [43] M. Ryle. A New Radio Interferometer and Its Application to the Observation of Weak Radio Stars. *Proceedings of the Royal Society of London Series A*, 211:351–375, March 1952.
- [44] M. Ryle. The 5-km Radio Telescope at Cambridge. *Nature*, 239:435–438, October 1972.
- [45] M. Ryle, B. Elsmore, and A. C. Neville. High-Resolution Observations of the Radio Sources in Cygnus and Cassiopeia. *Nature*, 205:1259–1262, March 1965.
- [46] M. Ryle and D. D. Vonberg. Solar Radiation on 175 Mc./s. *Nature*, 158:339–340, September 1946.
- [47] F. G. Smith. An Accurate Determination of the Positions of Four Radio Stars. *Nature*, 168:555, September 1951.
- [48] F. G. Smith. The determination of the position of a radio star. *MNRAS*, 112:497, 1952.
- [49] F. G. Smith. The Measurement of the Angular Diameter of Radio Stars. *Proceedings of the Physical Society B*, 65:971–980, December 1952.
- [50] A. R. Thompson, B. G. Clark, C. M. Wade, and P. J. Napier. The Very Large Array. *ApJS*, 44:151–167, October 1980.
- [51] A. R. Thompson, J. M. Moran, and G. W. Swenson. *Interferometry and synthesis in radio astronomy*. 1986.
- [52] R. C. Walker, P. E. Hardee, F. Davies, C. Ly, W. Junor, F. Mertens, and A. Lobanov. Observations of the Structure and Dynamics of the Inner M87 Jet. *Galaxies*, 4:46, October 2016.
- [53] A. R. Whitney, A. E. E. Rogers, H. F. Hinteregger, C. A. Knight, J. I. Levine, S. Lippincott, T. A. Clark, I. I. Shapiro, and D. S. Robertson. A very-long-baseline interferometer system for geodetic applications. *Radio Science*, 11:421–432, May 1976.
- [54] A. Wootten and A. R. Thompson. The Atacama Large Millimeter/Submillimeter Array. *IEEE Proceedings*, 97:1463–1471, August 2009.